



Larmor precession in strongly correlated itinerant electron systems

Erik G. C. P. van Loon ¹✉ & Hugo U. R. Strand ^{2,3}✉

Many-electron systems undergo a collective Larmor precession in the presence of a magnetic field. In a paramagnetic metal, the resulting spin wave provides insight into the correlation effects generated by the electron-electron interaction. Here, we use dynamical mean-field theory to investigate the collective Larmor precession in the strongly correlated regime, where dynamical correlation effects such as quasiparticle lifetimes and non-quasiparticle states are essential. We study the spin excitation spectrum, which includes a dispersive Larmor mode as well as electron-hole excitations that lead to Stoner damping. We also extract the momentum-resolved damping of slow spin waves. The accurate theoretical description of these phenomena relies on the Ward identity, which guarantees a precise cancellation of self-energy and vertex corrections at long wavelengths. Our findings pave the way towards a better understanding of spin wave damping in correlated materials.

¹NanoLund and Division of Mathematical Physics, Department of Physics, Lund University, Lund, Sweden. ²School of Science and Technology, Örebro University, SE-701 82 Örebro, Sweden. ³Institute for Molecules and Materials, Radboud University, 6525 AJ Nijmegen, the Netherlands. ✉email: erik.van_loon@teorfys.lu.se; hugo.strand@oru.se

Magnetization dynamics is a field with great technological and scientific importance, with topics ranging from magnetic data storage^{1,2} to magnetic skyrmions³, the ultrafast optical manipulation of magnetism^{4,5}, and the properties of earth's core⁶. Although magnetization dynamics in solids is frequently modeled using localized magnetic moments⁷, it fundamentally originates from the electrons and their quantum mechanical delocalization and Coulomb interaction. The description in terms of immobile moments is a particularly drastic approximation for metals with itinerant electrons.

The application of an external magnetic field leads to spin waves in paramagnetic metals. The dispersion relation of the spin wave $\omega_L(\mathbf{q})$ has a universal value at zero momentum $\mathbf{q} = \mathbf{0}$, corresponding to the Larmor precession of the system's total magnetic moment, while $\omega_L(\mathbf{q})$ depends on the interactions and correlations in the system at finite \mathbf{q} ^{8–12}. In a Fermi liquid, conduction-electron spin resonance experiments in the presence of a magnetic field can be used to extract the magnetic Landau parameters B_0, B_1 based on this effect^{10,13}, which was a crucial confirmation of Fermi liquid theory for the alkali metals in the late 1960s and early 1970s¹¹. Given the current interest in and limited understanding of non-Fermi liquid behavior in correlated electron systems^{14,15}, similar studies of spin waves in the presence of a magnetic field have the potential to provide additional insight.

In addition to the dispersion, there is also the question of spin wave damping. For systems with $SU(2)$ spin symmetry, the uniform Larmor precession is undamped, so the damping of the associated spin wave should vanish at long wavelengths ($\mathbf{q} \rightarrow \mathbf{0}$)¹¹, similar to plasmons¹⁶. At finite wavelength ($|\mathbf{q}| > 0$), the collective mode can be damped by electron–hole excitations (Stoner/Landau damping¹⁶) and the finite quasiparticle lifetime of the interacting electrons, i.e., electron–electron scattering. The latter is a paradigmatic example of a correlation effect, making it hard to model adequately.

In this work, we study the magnetization dynamics and damping of spin waves in the Hubbard–Zeeman model (Fig. 1a). We use dynamical mean-field theory (DMFT)^{17,18} to handle strong correlations while maintaining the appropriate Ward identities^{19–21}. We show the importance of dynamical correlation effects for the spin excitation spectrum, leading to changes in the dispersion and the damping as well as the appearance of an additional spin wave mode.

Results

Larmor precession. A single magnetic moment in an external magnetic field $B\vec{e}_z$ will partially align itself with the magnetic field while the in-plane component undergoes Larmor precession with a characteristic frequency $\omega_L = B$. For a larger system composed of several electrons or magnetic moments, a similar precession occurs for the total magnetization $\vec{S}_T = \sum_a \vec{S}_a$. If the Hamiltonian without field H_0 is $SU(2)$ spin-symmetric, and $H = H_0 - BS_T^z$, then the Heisenberg equation of motion for the total magnetization and the precession frequency $\omega_L = B$ is identical to that of the single moment, independently of the details of the system (see Methods). Here, we have incorporated the g -factor into the definition of B , and we use $\hbar = 1$. The Larmor precession is undamped, a fact that follows directly from the Heisenberg equation of motion.

Hubbard model. We now consider the single-orbital Hubbard model on the square lattice, i.e., $H_0 = -t\sum_{(ab),\sigma} c_{a\sigma}^\dagger c_{b\sigma} + U\sum_a n_{a\uparrow} n_{a\downarrow}$, where $c_{a\sigma}^\dagger$ creates an electron on site a with spin $\sigma \in \{\uparrow, \downarrow\}$, $c_{a\sigma}$ is the corresponding annihilation operator, $n_{a\sigma} = c_{a\sigma}^\dagger c_{a\sigma}$ is a number operator, and the sum $\sum_{(ab)}$ goes over pairs of neighboring sites a, b . The local spin operator \vec{S}_a has components

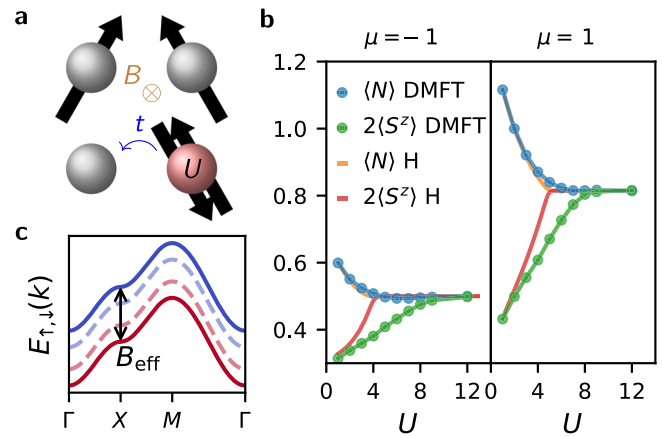


Fig. 1 The Hubbard–Zeeman model. **a** Electrons on a lattice with hopping parameter t , Hubbard interaction U and Zeeman magnetic field B . **b** Density $\langle N \rangle = \langle n_\uparrow \rangle + \langle n_\downarrow \rangle$ in the Hubbard–Zeeman model, calculated using dynamical mean-field theory (DMFT, blue) and the Hartree approximation (H, orange). Similarly, the magnetization $2\langle S^z \rangle = \langle n_\uparrow \rangle - \langle n_\downarrow \rangle$ in DMFT (green) and Hartree (red). Calculations with temperature $T = 1/10$, magnetic field $B = 2$, and chemical potential $\mu = \pm 1$. **c** Stoner enhancement of the band splitting. The interaction leads to an enhanced effective Zeeman field B_{eff} and, therefore, a larger splitting between the minority (solid blue) and the majority (solid red) bands $E_\uparrow(k), E_\downarrow(k)$ than in the non-interacting system (dashed blue and dashed red, respectively), where k is taken along the Γ -X-M- Γ high-symmetry path.

$S_a^\eta = \sum_{\sigma\sigma'} c_{a\sigma}^\dagger \sigma_{\sigma\sigma'}^\eta c_{a\sigma'}$, where $\sigma^\eta, \eta \in \{x, y, z\}$ are the Pauli matrices. The parameter t is the hopping matrix element, and U is the Coulomb repulsion between electrons on the same site. As U increases, the system becomes more and more correlated. The bandwidth is $8t$, and we use units of energy $t = 1$. We consider this model in thermodynamic equilibrium, in the grand canonical ensemble at fixed temperature $T = 1/\beta$, chemical potential μ , and magnetic field B . The simulations in the figures are for $T = 1/10$ and $B = 2$. The model is illustrated in Fig. 1a. The magnetization dynamics in equilibrium are encoded in the spatiotemporal correlation function $\chi(t, \mathbf{r}) = \langle S^x(t, \mathbf{r}) S^x(0, \mathbf{0}) \rangle$ and its Fourier transforms $\chi(\omega, \mathbf{q})$, which we call the susceptibility. We look at the spin components orthogonal to the field since these show the collective Larmor precession.

Using DMFT, we can calculate both the susceptibility defined above and single-particle properties such as the spectral function $A^\sigma(E, \mathbf{k})$ and the average density and magnetization, $\langle N \rangle$ and $\langle S^z \rangle$, which are shown in Fig. 1b. The DMFT calculations take into account (dynamical) correlation effects such as finite electronic lifetimes, bandwidth renormalization and spectral weight transfer, as well as the associated vertex corrections to the susceptibility. These vertex corrections are needed to satisfy the Ward identities, an exact relation between single-particle and two-particle properties. Only approximations that satisfy the Ward identities are guaranteed to find the undamped Larmor precession at the correct frequency^{19,21,22} (see “Methods”). Essentially, the Ward identities lead to a precise cancellation of self-energy effects and vertex corrections for the Larmor precession. We compare the resulting susceptibility to the random phase approximation (RPA). Via the Ward identities, the RPA corresponds to taking into account only static Hartree shifts in the band structure, and it is therefore only applicable to weakly correlated systems.

Moderate correlation. The electron–electron interaction U leads to a finite quasiparticle lifetime for electrons away from the Fermi

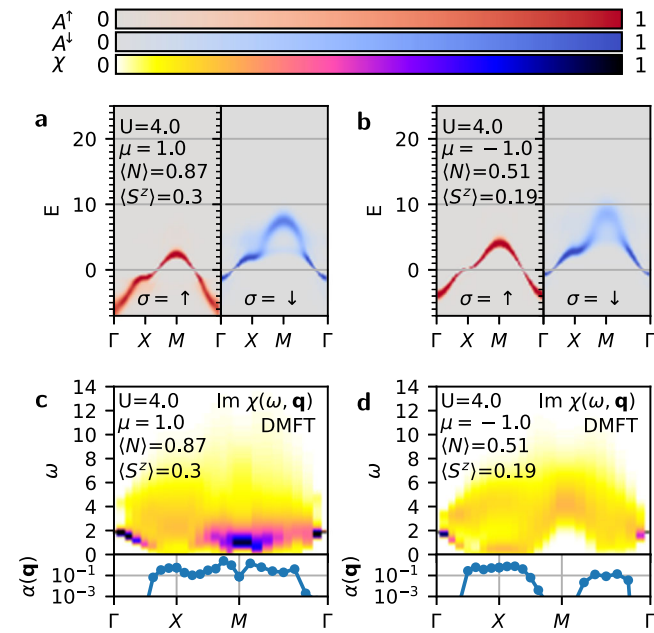


Fig. 2 Moderate correlation. **a, b** Single-particle spectral function $A^\sigma(E, \mathbf{k})$ at a Hubbard interaction $U = 4$ for chemical potential **a** $\mu = 1$ and **b** $\mu = -1$. The associated density $\langle N \rangle$ and magnetization $\langle S^z \rangle$ are indicated. **c, d** Susceptibility $\text{Im}\chi(\omega, \mathbf{q})$ and damping $\alpha(\mathbf{q}) = \partial \text{Im}\chi(\omega, \mathbf{q}) / \partial \omega|_{\omega=0}$ for **c** $\mu = 1$ and **d** $\mu = -1$. All momenta are taken along the Γ -X-M- Γ high-symmetry path. Calculations using dynamical mean-field theory (DMFT).

level, as is visible in the band broadening in Fig. 2a, b. Furthermore, there is a Stoner enhancement of the magnetic field (Fig. 1c), which would be given by $B_{\text{eff}} = B + 2U\langle S^z \rangle$ in the Hartree approximation. In fact, this static Hartree mean field overestimates the Stoner enhancement. A minority electron can be on a site precisely at times when there is no majority electron there. The inclusion of these dynamical correlations reduces the spin polarization $\langle S^z \rangle$, as is visible in Fig. 1b. This is a clear sign of the importance of dynamical correlations even at moderate interaction strengths. Finally, we note the spectral weight transfer away from the main minority spin band, visible in the spectral function $A^\downarrow(E, \mathbf{k})$ in Fig. 2a, b.

Looking at $\chi(\omega, \mathbf{q})$, the spin excitation at the Γ -point (i.e., $\mathbf{q} = \mathbf{0}$) is fixed at the bare Larmor frequency $\omega_L(\mathbf{0}) = B = 2$, as required by the Heisenberg equation of motion and as guaranteed by DMFT's Ward identities, see Fig. 2c, d. Universality is lost when moving away from Γ to finite momenta $|\mathbf{q}| > 0$. As in the Fermi liquid (see Supplementary Note 1), the Larmor mode disperses downwards, allowing for a determination of Landau parameters^{10,13} in principle. At the same time, the electron-hole continuum emanates at Γ from the renormalized frequency given by the effective field $B_{\text{eff}} = B + 2U\langle S^z \rangle$. Broadening of the Larmor mode due to finite electronic lifetimes is allowed for any $\mathbf{q} \neq \mathbf{0}$ and is clearly visible in Fig. 2c, d. Once the Larmor mode and the electron-hole continuum meet further away from Γ , the Larmor mode can decay into electron-hole pairs (the Stoner/Landau damping), and the mode broadens further. Deep in the Brillouin zone, there is a rich energy and momentum structure in χ reflecting the particular fermiology at a given filling, including low-energy modes that are indicative of a tendency toward magnetic ordering. Our DMFT simulations have a limited energy resolution and cannot resolve the details of these structures, but they are clearly visible in RPA, see Fig. 3. At the same time, RPA does overestimate this tendency towards magnetic ordering²³, which is reflected in the much larger low-energy spectral weight in the RPA susceptibility. Finally, Fig. 2c, d

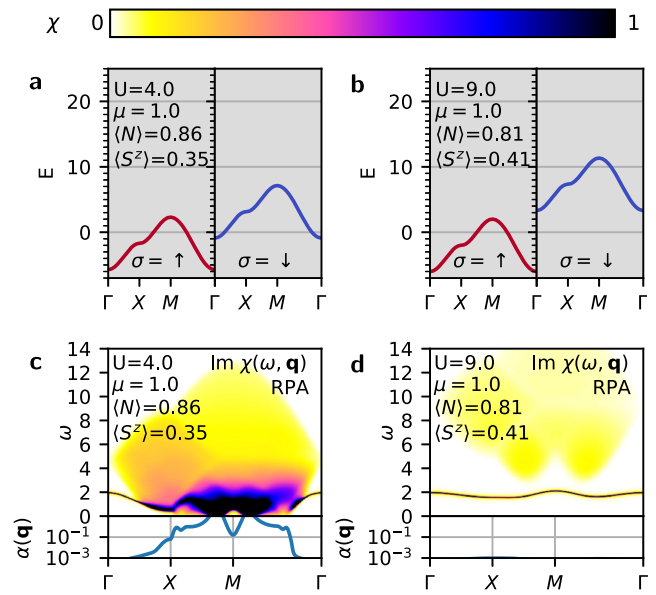


Fig. 3 Static mean-field. **a, b** Hartree approximation for the band structure at chemical potential $\mu = 1$ and a Hubbard interaction **a** $U = 4$ and **b** $U = 9$. Note that the bands are perfectly sharp in the Hartree approximation, so no color bar is shown. The associated density $\langle N \rangle$ and magnetization $\langle S^z \rangle$ are indicated. **c, d** Susceptibility $\text{Im}\chi(\omega, \mathbf{q})$ and damping $\alpha(\mathbf{q}) = \partial \text{Im}\chi(\omega, \mathbf{q}) / \partial \omega|_{\omega=0}$ for **c** $U = 4$ and **d** $U = 9$, calculated using the random phase approximation (RPA). All momenta are taken along the Γ -X-M- Γ high-symmetry path. Note that $\alpha(\mathbf{q}) < 10^{-3}$ for all momenta in (d).

also shows the low-frequency limit of the susceptibility, $\alpha(\mathbf{q})$, which will be discussed in more detail below. The relation to spin-wave spectra in systems with spontaneously broken symmetry²⁴ is discussed in Supplementary Note 2.

Strong correlation. At larger interaction strengths, the electronic structure changes qualitatively, as shown in Fig. 4a, b, becoming reminiscent of a ferromagnetic half-metal²⁵. Due to the large Stoner enhancement of the magnetic field, no minority electrons are present, visible as $\langle N \rangle \approx 2\langle S^z \rangle$ in Fig. 1b. As a result, the majority electrons move as free electrons according to their non-interacting band structure with very long lifetime (no band broadening). For the minority electrons, on the other hand, there are both quasiparticle states which are shifted to high energies due to the Stoner-enhanced field, and states just above the Fermi level where the minority and majority electrons move coherently so as to avoid doubly occupying a site. The electron-electron interaction also leads to scattering and, thus, to a finite lifetime of the minority electrons (band broadening). The precise structure of these features in the minority spectral function depends strongly on the chemical potential μ , which controls the filling of the majority band. A wider set of Hubbard interaction strengths is shown in Supplementary Note 3.

Studying $\chi(\omega, \mathbf{q})$ in Fig. 4c for $\mu = 1$, two electron-hole continua are visible close to Γ . One of them emanates from the expected high energy given by the effective magnetic field B_{eff} , while the one at lower energy originates from transitions between the majority band and the lower minority band. Thus, the spectral weight transfer at the single-particle level is reflected in the spin susceptibility, similar to the observation for plasmons²⁰. The appearance of this additional branch is an entirely dynamic correlation-driven effect that is beyond Hartree and the corresponding RPA. For $\mu = -1$ in Fig. 4b, d, the high-energy branch of the minority single-particle spectrum is very weak, and

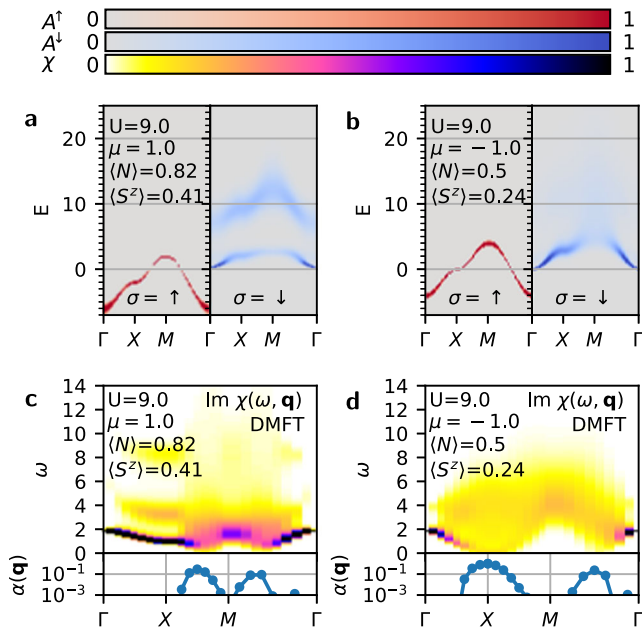


Fig. 4 Strong correlation. **a, b** Single-particle spectral function $A^\sigma(E, \mathbf{k})$ at a Hubbard interaction $U = 9$ for chemical potential **a** $\mu = 1$ and **b** $\mu = -1$. The associated density $\langle N \rangle$ and magnetization $\langle S^z \rangle$ are indicated. **c, d** Susceptibility $\text{Im}\chi(\omega, \mathbf{q})$ and damping $\alpha(\mathbf{q}) = \partial \text{Im}\chi(\omega, \mathbf{q}) / \partial \omega|_{\omega=0}$ for **c** $\mu = 1$ and **d** $\mu = -1$. All momenta are taken along the Γ -X-M- Γ high-symmetry path. Calculations using dynamical mean-field theory (DMFT).

as a result, there are also no high-energy excitations in the susceptibility at $B_{\text{eff}} \approx 6.3$.

Although $U = 9$ is clearly outside the formal range of applicability of RPA, it is worthwhile to consider how RPA fails by comparing Figs. 3d and 4c. The RPA incorrectly predicts an extremely sharp Larmor mode throughout the Brillouin Zone. The reason for this is that RPA only contains damping from electron-hole excitations, and it overestimates the energy of the minority electrons substantially since the Hartree band structure lacks the lower minority branch.

Weak correlation. For very small values of U , RPA is known to be accurate, and the comparison of RPA and DMFT can be used to assess the quality of the DMFT calculations. Figure 5 shows that both methods indeed give qualitatively similar results: low energy spectral weight in large parts of the Brillouin Zone except close to M, maximum energy $\omega \approx 6$ at X, and one upwards and one downwards dispersing mode close to Γ . Note that the Stoner enhancement $2U\langle S^z \rangle$ is so small that it is not possible to observe the splitting between the Larmor mode and the electron-hole continuum in either figure. We have a much better energy (and momentum) resolution in RPA, which makes it possible to resolve the sharp features that characterize electronic quasi-particles with a very long lifetime. Note that $U > 0$, so DMFT already contains some finite lifetime effects and should not be expected to match the RPA exactly.

Damping of slow modes. Low-energy (slow) magnetization dynamics can be described using the Landau-Lifshitz-Gilbert equation⁷, which contains the Gilbert damping as a parameter. In general, the Gilbert damping can be nonlocal, although it is frequently assumed to be local (\mathbf{q} -independent) for convenience. To connect magnetization dynamics to first-principles calculations, it is necessary to extract the damping parameter from an electronic model. Several mechanisms contribute to the damping of

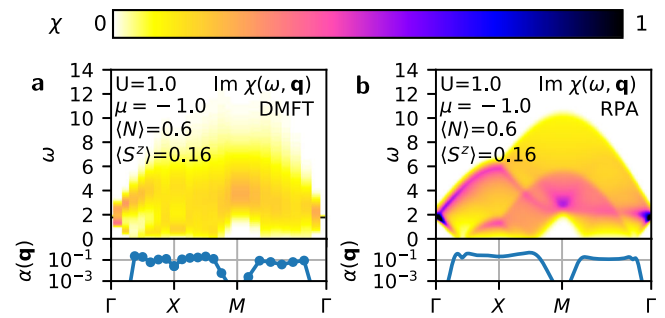


Fig. 5 Weak correlation. The susceptibility $\text{Im}\chi(\omega, \mathbf{q})$ and damping $\alpha(\mathbf{q}) = \partial \text{Im}\chi(\omega, \mathbf{q}) / \partial \omega|_{\omega=0}$ for **a** dynamical mean-field theory (DMFT) and **b** the random-phase approximation (RPA), both at Hubbard interaction $U = 1$ and chemical potential $\mu = -1$. The density $\langle N \rangle$, magnetization $\langle S^z \rangle$, susceptibility, and damping are similar in both approaches. Note that we are able to perform the RPA calculations with much higher energy resolution. All momenta are taken along the Γ -X-M- Γ high-symmetry path.

low-energy modes in real materials, including spin-orbit coupling, coupling to the lattice and impurities, decay of spin waves into electron-hole excitations, and finite electronic lifetimes. In our model, there is no spin-orbit coupling or coupling to the lattice or impurities by construction, which gives us a clear view of the physics of electron-hole excitations and finite electronic lifetimes. We should stress that spin-orbit coupling is the main damping mechanism for spin waves in many magnetic materials and can, in principle, be included in multi-orbital DMFT calculations. To connect our electronic model to slow magnetization dynamics^{26–28}, we study $\alpha(\mathbf{q}) = \frac{\partial \text{Im}\chi(\omega, \mathbf{q})}{\partial \omega}|_{\omega=0}$, which is shown below, the color maps in the $\text{Im}\chi(\omega, \mathbf{q})$ figures. Note that we show $\alpha(\mathbf{q})$ on a logarithmic scale with a lower cut-off at 10^{-3} .

Starting with the weakly correlated system, Fig. 5 shows the quantitative agreement of $\alpha(\mathbf{q})$ between DMFT and RPA. Since RPA is known to be accurate in this regime, this provides confidence in the numerical methods used to extract $\alpha(\mathbf{q})$ from the analytically continued DMFT spectra. At this small value of U , $\alpha(\mathbf{q})$ is relatively flat in a large part of the Brillouin Zone and quickly drops close to Γ . In RPA, the damping of slow modes $\alpha(\mathbf{q})$ is non-zero when the transferred momenta \mathbf{q} connects the minority and majority Fermi surfaces (see Supplementary Fig. 2) since that is where electron-hole damping at $\omega = 0$ is possible. For larger values of U , $\alpha(\mathbf{q})$ becomes more momentum-dependent, i.e., less local. We find that the RPA does not describe $\alpha(\mathbf{q})$ in moderately and strongly correlated systems accurately. It underestimates the damping by electron-hole excitations since it puts the electron-hole continuum too far away. At strong coupling, it also completely lacks the lower electron-hole excitation branch. As a result, at $U = 9$, the RPA predicts a negligible damping of slow modes even though the DMFT calculation shows a substantial damping deep in the Brillouin Zone. At moderate correlation strength, $U = 4$, the RPA overestimates the tendency towards magnetic ordering and thereby also $\alpha(\mathbf{q})$. For additional analysis of the structure of α in real space see Supplementary Note 4.

Energy scales. For clarity, we have illustrated the Larmor precession in situations where the Zeeman splitting is smaller than but comparable to the electronic bandwidth. In practice, the Bohr magneton $\mu_B = 5 \times 10^{-5}$ eV/T leads to sub-meV Larmor frequencies at realistic magnetic field strengths, substantially below the relevant electronic bandwidth in conventional materials. For that reason, the magnetization dynamics and electronic dynamics can frequently be considered as decoupled phenomena. On the

other hand, extremely narrow bands can be created in artificial superlattices, such as twisted bilayer graphene²⁹, transition metal dichalcogenide bilayers^{30–32}, and fermions in optical lattices³³. These systems are promising experimental platforms for studying the collective Larmor precession and the electron–hole continua.

Discussion

We have studied the collective Larmor precession of correlated electron systems in the presence of a Zeeman field. A comparison of RPA and DMFT calculations shows that dynamical correlation effects are crucial in the moderate and strong correlation regime for the dispersion and damping of the spin excitations as well as for the single-particle spectrum. The damping is due to a combination of Stoner damping by electron–hole excitations (present but underestimated in RPA), finite electronic lifetimes, and vertex corrections (both correlation effects beyond RPA). The DMFT susceptibility, however, can describe all of these effects since it satisfies the Ward identities. The resulting damping of slow modes by electronic excitations is strongly momentum-dependent.

Current state-of-the-art calculations of the damping of slow modes in the spin dynamics are restricted to static mean-field approximations^{7,28}. For this level of theory, the torque-torque correlator approach³⁴ is applicable for damping of spatially uniform spin excitations, i.e., at small momenta ($|\mathbf{q}| \approx 0$). However, in several canonical systems like Fe and Ni, many-body correlations beyond static mean-field are important^{6,35,36}, and they drastically influence the Gilbert damping²⁸. To account for these effects, ad hoc quasi-particle lifetimes have been introduced in the calculation of the mean-field torque-torque correlator^{28,34,37}. Formally this is equivalent to a calculation using the RPA where only the bubble susceptibility is independently modified to account for many-body effects on the single-particle level. However, this completely neglects vertex corrections on the two-particle level, which are a priori just as important, and breaks the Ward identities. It also does not take into account the splitting of the minority electron spectral function. These facts hinder quantitative calculations of the contribution of electronic processes to the Gilbert damping when electronic correlations are important.

For correlated metals like Fe and Ni, the quantitative calculation of Gilbert damping due to electron–electron scattering requires a consistent treatment of single-particle and two-particle correlation effects. In fact, a perfect cancellation of the two effects occurs in the long-wavelength limit as a consequence of the Ward identities. Hence, we conjecture that DMFT, which satisfies the Ward identity, is able to describe Gilbert damping due to electron–electron scattering accurately. A full account of Gilbert damping needs to take into account spin–orbit coupling as well since it is the dominant mechanism at long wavelengths and survives in the limit $\mathbf{q} \rightarrow 0$. Spin–orbit coupling can be taken into account in DMFT, so a generalization of the current set-up to multiorbital systems is able to incorporate this mechanism.

Methods

DMFT calculations. The numerical calculations in this work are based on the toolbox for research on interacting quantum systems (TRIQS)³⁸ and the two-particle response function toolbox (TPRF)³⁹. The DMFT self-consistency cycle was performed using continuous time hybridization expansion quantum Monte Carlo^{40–43} as implemented in TRIQS⁴⁴, while the two-particle correlation functions of the impurity model were calculated with worm sampling^{45,46} using the Wien/Würzburg strong coupling solver (W2Dynamics)⁴⁷. Worm sampling is needed to get access to the full orbital structure of the correlation functions. Based on these

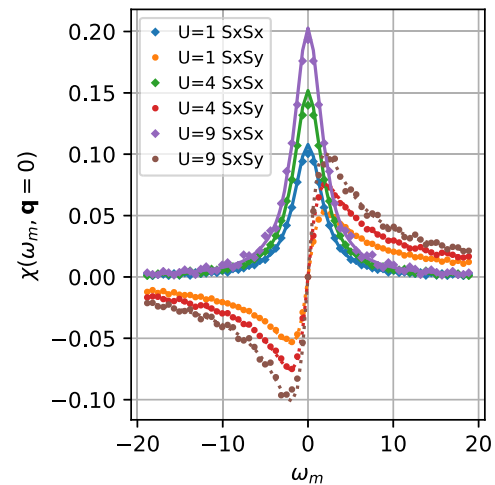


Fig. 6 Exact long-wavelength limit. Matsubara axis susceptibility $\chi(\omega_m, \mathbf{q} = 0)$ for several values of the Hubbard interaction U . The symbols show the calculated dynamical mean-field theory (DMFT) susceptibility, the lines are the exact result of Eq. (2). Both $\chi^{S^z S^z}$ and $\chi^{S^z S^y}$ are shown.

ingredients, we calculate the DMFT lattice susceptibility^{18,48–53}, using an efficient implementation⁵⁴ of the Bethe–Salpeter equation to improve the frequency convergence. This implementation corresponds to the dual boson version of the DMFT susceptibility^{19,55}, generalized to systems with inequivalent orbitals, and is called the dual Bethe–Salpeter equation (DBSE). This formalism uses the impurity susceptibility $\chi^{\text{imp}}(\omega_m)$, which in principle can be sampled in the worm CTM, but that turned out to be difficult to measure with sufficient accuracy due to ergodicity problems, especially at low frequency. Fortunately, $\chi(\omega_m, \mathbf{0})$ is known exactly (see below). Figure 6 shows the mismatch between the calculated and analytical susceptibility due to the uncertainty in χ^{imp} . We introduce a momentum-independent correction, $\chi^{\text{corrected}}(\omega, \mathbf{q}) = \chi(\omega, \mathbf{q}) + \chi^{\text{analytical}}(\omega, \mathbf{0}) - \chi(\omega, \mathbf{0})$ to enforce the exact result at $\mathbf{q} = 0$. This procedure is similar in spirit to the correction applied by Niyazi et al.²⁴, although $\chi^{\text{analytical}}$ is different in this case.

A momentum discretization of 16×16 is used for the DMFT and DMFT-DBSE calculations, which is sufficient for the chosen parameter regime. The single-particle spectral function $A^\sigma(E, \mathbf{k})$ is plotted on a denser momentum grid for visual purposes, this momentum-grid conversion is possible since Σ is local in DMFT.

We note that the calculations presented here take place above T_c , so DMFT’s problems with low-temperature spurious ordering⁵⁶ (at $B=0$) are not an issue. We checked that the leading eigenvalues of the DBSE are below unity to ensure that no ordering phase transition takes place.

The final part of the calculation is the maximum entropy (MaxEnt) analytical continuation⁵⁷ of the susceptibility $\chi^{\text{corrected}}(\omega_m, \mathbf{q})$ and the single-particle Green’s function from Matsubara to real frequency. For this, we use the Python package for analytic continuation (ana_cont)⁵⁸. Analytical continuation from Matsubara to real frequency data is an intrinsically hard computational problem, and many methods to perform the continuation have been discussed in the literature, also for susceptibilities (i.e., bosonic functions)^{59–61}. The result of an analytical continuation is, in some sense, only the most probable result consistent with the Matsubara data. Here, we have performed MaxEnt continuation with automatic tuning of the hyperparameter, as implemented in ana_cont. A constant noise amplitude of 10^{-3} is assumed for the susceptibility (10^{-2} for the spectral function), and results were checked to be qualitatively stable under variation of this parameter. A flat default model was assumed.

It is useful to discuss which features in our analytically continued spectra can be relied upon and which properties are more uncertain. Analytical continuation is especially difficult when the Matsubara data is subject to statistical noise, as in our DMFT calculations. Here, we have the advantage that we know the analytical form at $\mathbf{q} = 0$, and we have used this to remove the dominant Monte Carlo uncertainty (see above). Thereby, we recover the expected sharp Larmor peak at $\mathbf{q} = 0$. We also observe the correct number of spin excitation branches based on the single-particle spectra. The continuation at different momenta is performed independently, and the lack of discontinuities is a good sign for the quality of the continuation. On the other hand, the continuation is likely to blur sharp structures within a region of finite spectral weight, making it hard to identify possible splitting within the collective modes⁶² that has been discussed for charge fluctuations in the Hubbard model. Analytical continuation is known to be more reliable at low energies than at high energies. This makes the extraction of $\alpha(\mathbf{q})$ relatively safe. On the other hand, in Fig. 4b at $\mu = -1$, very diffuse high-energy weight is observed in $A^\downarrow(E, \mathbf{k})$ and no spectral weight is observed in $\text{Im}\chi(\omega, \mathbf{q})$ in Fig. 4d. Given the limitations of analytical continuation, it is hard to rule out that the true $\text{Im}\chi(\omega, \mathbf{q})$ at these parameters has a small amount of high-energy spectral weight.

RPA calculations. We have also calculated the susceptibility in the RPA. This takes into account the Hartree renormalization of the band structure and the corresponding static, unrenormalized vertex only, making it inapplicable in the strongly correlated regime. It has the advantage that exact, high-resolution simulations can be done easily, so it is valuable as a reference. DMFT, on the other hand, includes local dynamical correlations, including finite electronic lifetime effects and a local dynamical vertex, so it can describe the strong correlations that we are interested in here. DMFT simulations are computationally more expensive and require analytical continuation (see above), substantially limiting the attainable energy resolution. We note that both the RPA and DMFT susceptibilities satisfy the Ward identities, which guarantees exact relations at long wavelengths, where Larmor precession takes place. Supplementary Note 1 contains a study of the homogeneous electron gas using RPA, which clearly illustrates the physical content of the approximation.

Larmor precession. General properties of many-body Larmor precession in the presence of a Zeeman field have been studied in several works, see, e.g., Refs. 11,12,22. Here, we provide the necessary derivations in a form that closely matches the DMFT results presented in this work.

For a lattice model, Larmor precession in the presence of a Zeeman field occurs for the total magnetization $\vec{S}_T = \sum_a \vec{S}_a$, where \vec{S}_a is the spin on site a and the sum runs over the entire lattice. We consider a Hamiltonian $\hat{H} = \hat{H}_0 - B\vec{S}_T^z$, where H_0 is the $SU(2)$ symmetric Hamiltonian without the field; we have incorporated the g -factor into the definition of B , and $\hbar = 1$. The Heisenberg equation of motion for the total magnetization (\vec{S}_T) is identical to that of a single magnetic moment

$$\begin{aligned} \frac{d}{dt} \langle \hat{S}_T^x \rangle &= i \langle [\hat{H}, \hat{S}_T^x] \rangle = -iB \langle [\hat{S}_T^z, \hat{S}_T^x] \rangle = B \langle \hat{S}_T^y \rangle, \\ \frac{d}{dt} \langle \hat{S}_T^y \rangle &= -B \langle \hat{S}_T^x \rangle, \\ \frac{d^2}{dt^2} \langle \hat{S}_T^x \rangle &= -B^2 \langle \hat{S}_T^x \rangle, \end{aligned} \quad (1)$$

giving the precession frequency $\omega_L = B$. Note that the relation $\omega_L = B$ for the precession of the total magnetization is completely

independent of the total number of electrons, the lattice structure, and the Coulomb interaction between the electrons.

In this work, we study many electron systems on a lattice at finite temperatures, i.e., in a statistical ensemble. For such a statistical ensemble, $\langle S^x \rangle = 0$ at any time by symmetry. The Larmor precession is visible in the periodicity of the time-dependent spin correlation function. Since the total spin S_T processes with the same frequency ω_L in all the members of the ensemble, the dynamical total spin-total spin correlation function has a single sharp, undamped mode at the frequency $\omega = \pm \omega_L = \pm B$.

Since it relates to the total spin, the Larmor mode is visible at the momentum $\mathbf{q} = \mathbf{0}$ of the dynamical, momentum-dependent susceptibility. We use the general notation $\chi^{AB}(\omega, \mathbf{q}) = \langle AB \rangle_{\omega, \mathbf{q}} - \delta_\omega \delta_{\mathbf{q}} \langle A \rangle \langle B \rangle$ to denote susceptibilities corresponding to different observables A, B . We use both real frequencies ω and Matsubara frequencies $i\omega_m$ for the retarded and Matsubara correlation functions, respectively. In the main text, $A = B = S^x$, and the superscript is dropped for clarity. We also note that χ is sometimes defined with an overall minus sign, e.g., Giuliani and Vignale¹⁶ or Krien et al.²¹, which requires some care when comparing formulas with the literature.

The exact form of the dynamical spin susceptibility at $\mathbf{q} = \mathbf{0}$ is²²

$$\chi^{S^x S^x}(\omega, \mathbf{0}) = \frac{B \langle S_z \rangle}{B^2 - \omega^2}, \quad (2)$$

$$\chi^{S^x S^y}(\omega, \mathbf{0}) = -\frac{i\omega \langle S_z \rangle}{B^2 - \omega^2}. \quad (3)$$

The location of the two poles in the complex ω plane is known from the equation of motion, and their residue will be derived below using formulas for the large-frequency asymptotics. Both expressions are exact since they are derived from the equation of motion without approximation. They depend explicitly on B and implicitly on all other system parameters via $\langle S^z \rangle$, which only determine the overall magnitude. Note that there is no discontinuous δ_ω contribution^{19,63} to $\chi^{S^x S^x}$, since S^x is not a conserved quantity in the presence of a Zeeman field. For $\mathbf{q} \neq \mathbf{0}$, the equation of motion generates additional terms $[H_0, S_{\mathbf{q}}^x]$, which leads to a dispersion relation $\omega_L(\mathbf{q})$ that is sensitive to details of the system¹¹.

Larmor precession: magnitude of susceptibility. The frequency structure of the Larmor precession follows directly from the equation of motion. Here, we derive the magnitude of the susceptibility in the Matsubara formalism. The susceptibility is known to decay algebraically at large Matsubara frequencies, and the prefactors of this asymptotic decay are given by commutation relations^{21,64}. For a general susceptibility χ^{AB} , the leading asymptotic Matsubara decay (first moment) is determined by the commutator $[A, B]$, i.e., $i\omega_m \chi^{AB}(i\omega_m) \rightarrow \langle [A, B] \rangle$ for $|\omega_m| \rightarrow \infty$. The relevant case for us is $[S^x, S^y] = iS^z$,

$$\chi^{S^x S^y}(i\omega_m, \mathbf{0}) \stackrel{|\omega_m| \rightarrow \infty}{\sim} \langle S^z \rangle / \omega_m. \quad (4)$$

For $\chi^{S^x S^x}$ and $\chi^{S^y S^y}$, where $A = B$, this commutator vanishes, and the next term in the asymptotic expansion is $(i\omega_m)^2 \chi^{AB}(i\omega_m) \rightarrow -\langle [[A, H], B] \rangle$. Since H appears linearly, the high-frequency tail coefficient can be decomposed into contributions from the interaction, the dispersion, and the Zeeman field. In the present case, the interaction does not contribute, while the dispersion leads to a coefficient related to $\partial^2 \epsilon_k / \partial k^2$ and is the same for $\chi^{S^x S^x}$ and $\chi^{S^y S^y}$. This term is \mathbf{q} -dependent with a vanishing value at $\mathbf{q} = \mathbf{0}$. Finally, the Zeeman field is not relevant

for $\chi^{S^x S^x}$ but is relevant for $\chi^{S^x S^y}$, where it creates a local term (independent of \mathbf{q}). Since this is the only contribution at $\mathbf{q} = 0$, using $[[S^x, -BS^z], S^x] = iB[S^y, S^x] = BS^z$, we get

$$(i\omega_m)^2 \chi^{S^x S^x}(i\omega_m, \mathbf{0}) \stackrel{|\omega_m| \rightarrow \infty}{=} -B\langle S^z \rangle. \quad (5)$$

Higher-order moments of the susceptibility are obtained by inserting additional commutators with the Hamiltonian, i.e.,

$$[[[S^x, H], H], S^x] = B^2[[[S^x, S^z], S^z], S^x] = 0 \quad (6)$$

$$\begin{aligned} [[[[S^x, H], H], H], S^x] &= -B^3[[[S^x, S^z], S^z], S^x] \\ &= -B^3(-i)[[S^y, S^z], S^x] \\ &= -B^3[[S^x, S^z], S^x] \\ &= -B^3(-i)[S^y, S^x] \\ &= B^3 S^z. \end{aligned} \quad (7)$$

Since the only non-commuting part of the Hamiltonian is $-BS^z$, every additional commutator leads to a switch between S^x and S^y and a factor $+i$ or $-i$. Thus, for $\chi^{S^x S^y}$, only the odd commutators survive, and the moment expansion is

$$\begin{aligned} \chi^{S^x S^y}(i\omega_m, \mathbf{0}) &= -\frac{B\langle S^z \rangle}{(i\omega_m)^2} \sum_{M=0}^{\infty} \frac{B^{2M}}{(i\omega_m)^{2M}} \\ &= -\frac{B\langle S^z \rangle}{(i\omega_m)^2 - B^2}. \end{aligned} \quad (8)$$

By analytical continuation $i\omega_m \rightarrow \omega$, this completes the proof of Eq. (2).

Note that the magnitudes of $\chi^{S^x S^x}$ and $\chi^{S^x S^y}$ are linked, since the corresponding observables are governed by the coupled differential equations in Eq. (1). Using $2S^x = S^+ + S^-$, $2iS^y = S^+ - S^-$, Eq. (2) implies that $\chi^{+}(\omega, \mathbf{0})$ and $\chi^{-}(\omega, \mathbf{0})$ each has a single simple pole, at $\omega = +\omega_L = +B$ and $\omega = -\omega_L = -B$, respectively. These two susceptibilities are related by time-reversal symmetry and $B \mapsto -B$. The commutation relation $[S^+, S^-] = 2S^z$ constrains the instantaneous two-particle correlation functions (that is, the integral over ω of Eq. (2)) in terms of the one-particle expectation value $\langle S^z \rangle$, and gives a simple explanation for the appearance of $\langle S^z \rangle$ on the right-hand side of Eq. (2).

Larmor precession: limits. It is useful to verify Eq. (2) in several relevant limits; see also the discussion in refs. 22,24. The limit $\omega \rightarrow 0$ of a dynamic susceptibility is the linear response to an applied field. Here, starting with $B\hat{e}_z$ and applying a small field $\delta B\hat{e}_x$ does not change the magnitude of the field to linear order in δB , but it changes its orientation to $B\hat{e}_z + \delta B\hat{e}_x$, again, keeping terms to linear order in δB only. The magnetization will follow this orientation, so $\delta\langle S^x \rangle = \frac{\delta B}{B}\langle S^z \rangle$. In other words, $\frac{d\langle S^x \rangle}{dB} = \frac{\langle S^z \rangle}{B} = \chi^{S^x S^x}(0, \mathbf{0})$, consistent with Eq. (2).

If we now take the limit $B \rightarrow 0$, we recover $\chi^{S^x S^x}(0, \mathbf{0}) = \frac{d\langle S^x \rangle}{dB} = \chi^{S^z S^z}(0, \mathbf{0})$, as expected since the Hamiltonian is $SU(2)$ symmetric in this limit, and we are considering a paramagnetic state. Furthermore, the poles in $\chi^{S^x S^x}$ move toward the real axis and at $B = 0$, $\chi^{S^x S^x}(\omega, \mathbf{0}) \propto \delta_\omega$ as usual for a conserved quantity.

Hartree and RPA. The susceptibility in the non-interacting model is given by the Lindhard bubble; for the spin-flip channel, it is

$$\hat{\chi}_0^{+}(\omega, \mathbf{q}) = \sum_{\mathbf{k}} \frac{n_{\mathbf{k}+\mathbf{q}}^{\downarrow} - n_{\mathbf{k}}^{\uparrow}}{\omega - E_{\mathbf{k}+\mathbf{q}}^{\downarrow} + E_{\mathbf{k}}^{\uparrow}}. \quad (9)$$

At $\mathbf{q} = 0$, the denominator simplifies to $E^{\downarrow} - E^{\uparrow} = B$ independent of \mathbf{k} , so the momentum sum can be performed to give $\hat{\chi}_0^{+}(\omega, \mathbf{q} = 0) = -2\langle S^z \rangle/(\omega - B)$. By symmetry, $\hat{\chi}_0^{-}(\omega, \mathbf{q} = 0) = +2\langle S^z \rangle/(\omega - B)$, giving the expected result

$$\hat{\chi}_0^{S^x S^x}(\omega, \mathbf{q} = 0) = \frac{\hat{\chi}_0^{-+} + \hat{\chi}_0^{+-}}{4} = \frac{B\langle S^z \rangle}{B^2 - \omega^2}, \quad (10)$$

$$\hat{\chi}_0^{S^x S^y}(\omega, \mathbf{q} = 0) = \frac{\hat{\chi}_0^{-+} - \hat{\chi}_0^{+-}}{4i} = \frac{-i\omega\langle S^z \rangle}{B^2 - \omega^2}. \quad (11)$$

The effect of the Hubbard interaction at weak coupling can be studied within the Hartree approximation, which is exact to linear order in the interaction (the Fock self-energy is zero in the Hubbard model). The Hartree self-energy states that the electrons feel an effective additional on-site potential given by the density of the opposite spin, $\Sigma_\sigma = U\langle n_{-\sigma} \rangle$. The corresponding enhancement of the band splitting is $\Delta B^{\text{H}} = 2U\langle S^z \rangle$, leading to a larger magnetization. This is essentially just the Stoner mechanism^{7,16,25}. Note that this system of equations has to be solved self-consistently.

The RPA provides us with the dynamical susceptibilities associated with the Hartree single-particle energies. Due to the enhanced band splitting, $\hat{\chi}_0^{+}$ has its pole at $\omega = B + 2U\langle S^z \rangle > \omega_L$. The RPA susceptibility, written in a tensor formalism, is calculated from the Lindhard bubble via the Bethe-Salpeter equation $\hat{\chi}(\omega, \mathbf{q}) = \hat{\chi}_0(\omega, \mathbf{q}) + \hat{\chi}_0(\omega, \mathbf{q}) * \hat{U} * \hat{\chi}(\omega, \mathbf{q})$, where $\hat{\chi}_0$ is the Lindhard bubble. Importantly, the RPA also does not couple different momenta, so the analysis only requires the Lindhard bubble at $\mathbf{q} = 0$. The χ^{-} channel does not couple to other channels, and the Hubbard interaction enhances the magnetic susceptibility (Stoner enhancement).

The solution of the Bethe-Salpeter equation is

$$\begin{aligned} \hat{\chi}(\omega, \mathbf{q}) &= \hat{\chi}_0(\omega, \mathbf{q}) \times [\hat{1} - \hat{U}\hat{\chi}_0(\omega, \mathbf{q})]^{-1}, \\ \hat{1} - \hat{U}\hat{\chi}_0(\omega, \mathbf{q} = 0) &\stackrel{\chi^{+}}{\rightarrow} 1 - U \frac{-2\langle S^z \rangle}{\omega - (B + 2U\langle S^z \rangle)} \\ &= \frac{\omega - B - 2U\langle S^z \rangle + 2U\langle S^z \rangle}{\omega - B - 2U\langle S^z \rangle} \\ &= \frac{\omega - B}{\omega - B - 2U\langle S^z \rangle}, \end{aligned} \quad (12)$$

$$\chi^{-}(\omega, \mathbf{q} = 0) = \frac{-2\langle S^z \rangle}{\omega - B - 2U\langle S^z \rangle} \times \frac{\omega - B - 2U\langle S^z \rangle}{\omega - B} = \frac{-2\langle S^z \rangle}{\omega - B}. \quad (13)$$

The final result for $\hat{\chi}$ indeed has a simple pole at the correct frequency $\omega_L = B$ and with the appropriate residue required by the equation of motion. The correct result arises from a cancellation between single-particle renormalization and vertex corrections. This cancellation holds more generally, as shown below.

Ward identity and Larmor frequency. In general, the Bethe-Salpeter equation is a matrix equation in fermionic frequency and momentum space. In the RPA, the frequency dependence is trivial: the vertex is frequency-independent, and the electronic propagators have the form of non-interacting electrons in the effective Hartree potential. In that case, the frequency sums can be performed analytically to give the Lindhard bubble. In DMFT, both the bubble $\hat{\chi}_0$ and the vertex $\hat{\Gamma}$ are matrices in fermionic frequency space, and analytical treatment of the susceptibility is generically hard. However, it is known that DMFT satisfies the Ward identities, and this is sufficient to derive

$\mathbf{q} = 0$ properties of the susceptibility^{19,21}, including the Larmor frequency²².

The Ward identities express the relation between one-particle and two-particle correlation functions that have to be satisfied according to the Heisenberg equation of motion. Here, we follow the derivation given in Appendix A of Krien et al.²¹, which can be generalized to systems with a Zeeman field by putting spin labels on the Green's function and dispersion in Eq. (A6) of Krien et al.²¹, and by noting that their X corresponds to our $-\hat{\chi}$. Below, ν and ω are Matsubara frequencies. Note that the Zeeman field acts as a single-particle term, so $[\rho, H_{\text{int}}]$ still vanishes for the relevant susceptibility. Thus, the resulting Ward identity is

$$G_{\nu+\omega, \mathbf{k}+\mathbf{q}}^{\downarrow} - G_{\nu, \mathbf{k}}^{\uparrow} = - \sum_{\mathbf{k}', \nu'} \hat{\chi}_{\nu\nu'+\omega, \mathbf{k}\mathbf{k}+\mathbf{q}} \left[\epsilon_{\mathbf{k}'+\mathbf{q}}^{\downarrow} - \epsilon_{\mathbf{k}'}^{\uparrow} - i\omega \right]. \quad (14)$$

We get our desired result for the Larmor frequency by setting $\mathbf{q} = 0$ and summing over \mathbf{k} and ν . On the left-hand side, the momentum and frequency sums generate expectation values, i.e., $\sum_{\mathbf{k}\nu} G_{\mathbf{k}\nu}^{\uparrow} = \langle n_{\uparrow} \rangle$, while on the right-hand side $\epsilon_{\mathbf{k}+\mathbf{q}}^{\downarrow} - \epsilon_{\mathbf{k}}^{\uparrow} = B$. Altogether,

$$\langle n_{\downarrow} \rangle - \langle n_{\uparrow} \rangle = -\chi^{-+}(i\omega, \mathbf{0}) \times [B - i\omega] \quad (15)$$

$$\chi^{-+}(i\omega, \mathbf{0}) = -\frac{2\langle S^z \rangle}{i\omega - B} \quad (16)$$

Thus, any approximation that satisfies the Ward identities has the correct Larmor frequency. This includes both RPA and DMFT.

Data availability

The data that support the findings of this study are available from the corresponding author upon reasonable request.

Code availability

The Python code to perform DMFT calculations for the Hubbard–Zeeman model is made available at⁶⁵.

Received: 12 April 2023; Accepted: 4 October 2023;

Published online: 13 October 2023

References

- Baibich, M. N. et al. Giant magnetoresistance of (001)Fe/(001)Cr magnetic superlattices. *Phys. Rev. Lett.* **61**, 2472–2475 (1988).
- Binasch, G., Grünberg, P., Saurenbach, F. & Zinn, W. Enhanced magnetoresistance in layered magnetic structures with antiferromagnetic interlayer exchange. *Phys. Rev. B* **39**, 4828–4830 (1989).
- Fert, A., Reyren, N. & Cros, V. Magnetic skyrmions: advances in physics and potential applications. *Nat. Rev. Mater.* **2**, 1–15 (2017).
- Beaurepaire, E., Merle, J.-C., Daunois, A. & Bigot, J.-Y. Ultrafast spin dynamics in ferromagnetic nickel. *Phys. Rev. Lett.* **76**, 4250–4253 (1996).
- Kirilyuk, A., Kimel, A. V. & Rasing, T. Ultrafast optical manipulation of magnetic order. *Rev. Mod. Phys.* **82**, 2731–2784 (2010).
- Hausoel, A. et al. Local magnetic moments in iron and nickel at ambient and earth's core conditions. *Nat. Commun.* **8**, 16062 (2017).
- Eriksson, O., Bergman, A., Bergqvist, L. & Hellsvik, J. *Atomistic Spin Dynamics: Foundations and Applications* (Oxford University Press, 2017).
- Silin, V. Oscillations of a Fermi-liquid in a magnetic field. *Sov. Phys. JETP* **6**, 945–950 (1958).
- Silin, V. *Sov. Phys. JETP* **8**, 870 (1959).
- Platzman, P. M. & Wolff, P. A. Spin-wave excitation in nonferromagnetic metals. *Phys. Rev. Lett.* **18**, 280–283 (1967).
- Platzman, P. M. & Wolff, P. A. *Waves and Interactions In Solid State Plasmas*, vol. 13 (Academic Press New York, 1973).
- Oshikawa, M. & Affleck, I. Electron spin resonance in $S = \frac{1}{2}$ antiferromagnetic chains. *Phys. Rev. B* **65**, 134410 (2002).
- Schultz, S. & Dunifer, G. Observation of spin waves in sodium and potassium. *Phys. Rev. Lett.* **18**, 283–287 (1967).
- Phillips, P. W., Hussey, N. E. & Abbamonte, P. Stranger than metals. *Science* **377**, eabh4273 (2022).
- Chowdhury, D., Georges, A., Parcollet, O. & Sachdev, S. Sachdev-Ye-Kitaev models and beyond: window into non-Fermi liquids. *Rev. Mod. Phys.* **94**, 035004 (2022).
- Giuliani, G. & Vignale, G. *Quantum Theory of the Electron Liquid* (Cambridge University Press, 2005).
- Metzner, W. & Vollhardt, D. Correlated lattice fermions in $d = \infty$ dimensions. *Phys. Rev. Lett.* **62**, 324–327 (1989).
- Georges, A., Kotliar, G., Krauth, W. & Rozenberg, M. J. Dynamical mean-field theory of strongly correlated fermion systems and the limit of infinite dimensions. *Rev. Mod. Phys.* **68**, 13–125 (1996).
- Hafermann, H., van Loon, E. G. C. P., Katsnelson, M. I., Lichtenstein, A. I. & Parcollet, O. Collective charge excitations of strongly correlated electrons, vertex corrections, and gauge invariance. *Phys. Rev. B* **90**, 235105 (2014).
- van Loon, E. G. C. P., Hafermann, H., Lichtenstein, A. I., Rubtsov, A. N. & Katsnelson, M. I. Plasmons in strongly correlated systems: Spectral weight transfer and renormalized dispersion. *Phys. Rev. Lett.* **113**, 246407 (2014).
- Krien, F. et al. Conservation in two-particle self-consistent extensions of dynamical mean-field theory. *Phys. Rev. B* **96**, 075155 (2017).
- Krien, F. *Conserving Dynamical Mean-field Approaches to Strongly Correlated Systems*. Ph.D. thesis. (Staats- und Universitätsbibliothek Hamburg Carl von Ossietzky, 2018).
- Vilk, Y. & Tremblay, A.-M. Non-perturbative many-body approach to the Hubbard model and single-particle pseudogap. *J. Phys. I* **7**, 1309–1368 (1997).
- Niyazi, A., Geffroy, D. & Kuneš, J. Antiferromagnetic magnons and local anisotropy: dynamical mean-field study. *Phys. Rev. B* **104**, 075152 (2021).
- Katsnelson, M. I., Irkhin, V. Y., Chioncel, L., Lichtenstein, A. I. & de Groot, R. A. Half-metallic ferromagnets: from band structure to many-body effects. *Rev. Mod. Phys.* **80**, 315–378 (2008).
- Gilmore, K. *Precession Damping in Itinerant Ferromagnets*. Ph.D. thesis. (Montana State University, 2007).
- Umetsu, N., Miura, D. & Sakuma, A. Theoretical study on Gilbert damping of nonuniform magnetization precession in ferromagnetic metals. *J. Phys. Soc. Jpn.* **81**, 114716 (2012).
- Thonig, D., Kvashnin, Y., Eriksson, O. & Pereiro, M. Nonlocal Gilbert damping tensor within the torque-torque correlation model. *Phys. Rev. Mater.* **2**, 013801 (2018).
- Bistrizter, R. & MacDonald, A. H. Moiré bands in twisted double-layer graphene. *Proc. Natl Acad. Sci. USA* **108**, 12233–12237 (2011).
- Wu, F., Lovorn, T., Tutuc, E. & MacDonald, A. H. Hubbard model physics in transition metal dichalcogenide moiré bands. *Phys. Rev. Lett.* **121**, 026402 (2018).
- Tang, Y. et al. Simulation of Hubbard model physics in WSe₂/WS₂ moiré superlattices. *Nature* **579**, 353–358 (2020).
- Li, T. et al. Continuous Mott transition in semiconductor moiré superlattices. *Nature* **597**, 350–354 (2021).
- Esslinger, T. Fermi-Hubbard physics with atoms in an optical lattice. *Annu. Rev. Condens. Matter Phys.* **1**, 129–152 (2010).
- Kamberský, V. On ferromagnetic resonance damping in metals. *Czechoslov. J. Phys. B* **26**, 1366–1383 (1976).
- Lichtenstein, A. I., Katsnelson, M. I. & Kotliar, G. Finite-temperature magnetism of transition metals: an ab initio dynamical mean-field theory. *Phys. Rev. Lett.* **87**, 067205 (2001).
- Katanin, A. A., Belozero, A. S., Lichtenstein, A. I. & Katsnelson, M. I. Exchange interactions in iron and nickel: DFT + DMFT study in paramagnetic phase. *Phys. Rev. B* **107**, 235118 (2023).
- Gilmore, K., Idzerda, Y. U. & Stiles, M. D. Identification of the dominant precession-damping mechanism in Fe, Co, and Ni by first-principles calculations. *Phys. Rev. Lett.* **99**, 027204 (2007).
- Parcollet, O. et al. Triqs: A toolbox for research on interacting quantum systems. *Comput. Phys. Commun.* **196**, 398–415 (2015).
- Strand, H. U. R. Two-particle response function tool-box (TPRF) for TRIQS. <https://github.com/TRIQS/tprf> (2019).
- Werner, P. & Millis, A. J. Hybridization expansion impurity solver: general formulation and application to Kondo lattice and two-orbital models. *Phys. Rev. B* **74**, 155107 (2006).
- Werner, P., Comanac, A., de' Medici, L., Troyer, M. & Millis, A. J. Continuous-time solver for quantum impurity models. *Phys. Rev. Lett.* **97**, 076405 (2006).
- Haule, K. Quantum Monte Carlo impurity solver for cluster dynamical mean-field theory and electronic structure calculations with adjustable cluster base. *Phys. Rev. B* **75**, 155113 (2007).
- Gull, E. et al. Continuous-time Monte Carlo methods for quantum impurity models. *Rev. Mod. Phys.* **83**, 349–404 (2011).

44. Seth, P., Krivenko, I., Ferrero, M. & Parcollet, O. TRIQS/CTHYB: a continuous-time quantum Monte Carlo hybridisation expansion solver for quantum impurity problems. *Comput. Phys. Commun.* **200**, 274–284 (2016).
45. Gunacker, P. et al. Continuous-time quantum Monte Carlo using worm sampling. *Phys. Rev. B* **92**, 155102 (2015).
46. Gunacker, P. et al. Worm-improved estimators in continuous-time quantum Monte Carlo. *Phys. Rev. B* **94**, 125153 (2016).
47. Wallerberger, M. et al. w2dynamics: Local one- and two-particle quantities from dynamical mean field theory. *Comput. Phys. Commun.* **235**, 388 – 399 (2019).
48. Jarrell, M. Hubbard model in infinite dimensions: a quantum Monte Carlo study. *Phys. Rev. Lett.* **69**, 168–171 (1992).
49. Kuneš, J. Efficient treatment of two-particle vertices in dynamical mean-field theory. *Phys. Rev. B* **83**, 085102 (2011).
50. Boehnke, L., Hafermann, H., Ferrero, M., Lechermann, F. & Parcollet, O. Orthogonal polynomial representation of imaginary-time Green's functions. *Phys. Rev. B* **84**, 075145 (2011).
51. Boehnke, L. & Lechermann, F. Competing orders in Na_xCoO_2 from strong correlations on a two-particle level. *Phys. Rev. B* **85**, 115128 (2012).
52. Park, H., Haule, K. & Kotliar, G. Magnetic excitation spectra in BaFe_2As_2 : a two-particle approach within a combination of the density functional theory and the dynamical mean-field theory method. *Phys. Rev. Lett.* **107**, 137007 (2011).
53. Lin, N., Gull, E. & Millis, A. J. Two-particle response in cluster dynamical mean-field theory: Formalism and application to the Raman response of high-temperature superconductors. *Phys. Rev. Lett.* **109**, 106401 (2012).
54. van Loon, E. G. C. P. & Strand, H. U. R. Dual Bethe-Salpeter equation for the multi-orbital lattice susceptibility within dynamical mean-field theory. Preprint at *arXiv* <https://doi.org/10.48550/arXiv.2306.05157> (2023).
55. Rubtsov, A., Katsnelson, M. & Lichtenstein, A. Dual boson approach to collective excitations in correlated fermionic systems. *Ann. Phys.* **327**, 1320–1335 (2012).
56. Schäfer, T. et al. Fate of the false Mott-Hubbard transition in two dimensions. *Phys. Rev. B* **91**, 125109 (2015).
57. Jarrell, M. & Gubernatis, J. E. Bayesian inference and the analytic continuation of imaginary-time quantum Monte Carlo data. *Phys. Rep.* **269**, 133–195 (1996).
58. Kaufmann, J. & Held, K. ana_cont: Python package for analytic continuation. *Comput. Phys. Commun.* **282**, 108519 (2023).
59. Gunnarsson, O., Haverkort, M. W. & Sangiovanni, G. Analytical continuation of imaginary axis data for optical conductivity. *Phys. Rev. B* **82**, 165125 (2010).
60. Schött, J., van Loon, E. G. C. P., Loch, I. L. M., Katsnelson, M. I. & Di Marco, I. Comparison between methods of analytical continuation for bosonic functions. *Phys. Rev. B* **94**, 245140 (2016).
61. Huang, Z., Gull, E. & Lin, L. Robust analytic continuation of Green's functions via projection, pole estimation, and semidefinite relaxation. *Phys. Rev. B* **107**, 075151 (2023).
62. McNiven, B. D. E., Terletska, H., Andrews, G. T. & LeBlanc, J. P. F. One- and two-particle properties of the weakly interacting two-dimensional Hubbard model in proximity to the van Hove singularity. *Phys. Rev. B* **106**, 035145 (2022).
63. Watzenböck, C., Feller, M., Held, K. & Toschi, A. Long-term memory magnetic correlations in the Hubbard model: a dynamical mean-field theory analysis. *SciPost Phys.* **12**, 184 (2022).
64. Hügel, D., Werner, P., Pollet, L. & Strand, H. U. R. Bosonic self-energy functional theory. *Phys. Rev. B* **94**, 195119 (2016).
65. van Loon, E. G. C. P. & Strand, H. U. R. Larmor precession in strongly correlated itinerant electron systems. Code available on Zenodo: <https://doi.org/10.5281/zenodo.8203356> (2023).

Acknowledgements

The authors would like to acknowledge useful discussions with Danny Thonig, Olle Eriksson, Mikhail Katsnelson, and Simon Streib. Ev.L. acknowledges support from Gyllenstiernska Kräppstiftelsen, the Crafoord Foundation, and from the Swedish Research Council (Vetenskapsrådet, VR) under grant 2022-03090. Ev.L. also acknowledges support by eSENCE, a strategic research area for e-Science, grant number eSENCE@LU 9:1. HURS acknowledges funding from the European Research Council (ERC) under the European Union's Horizon 2020 research and innovation program (Grant agreement No. 854843-FASTCORR). The computations were enabled by resources provided by the Swedish National Infrastructure for Computing (SNIC) through the projects LU 2022/2-32, LU 2021/2-76, SNIC 2022/23-304, SNIC 2021/23-370, SNIC 2022/21-15, SNIC 2022/13-9, SNIC 2021/28-8, SNIC 2022/6-113, SNIC 2021/6-133, SNIC 2022/1-18, and SNIC 2021/1-36, at Lunarc, HPC2N, PDC, and NSC partially funded by the Swedish Research Council through grant agreement No. 2018-05973.

Author contributions

E.G.C.Pv.L. and H.U.R.S. contributed equally to the work.

Funding

Open access funding provided by Lund University.

Competing interests

The authors declare no competing interests.

Additional information

Supplementary information The online version contains supplementary material available at <https://doi.org/10.1038/s42005-023-01411-w>.

Correspondence and requests for materials should be addressed to Erik G. C. P. van Loon or Hugo U. R. Strand.

Peer review information *Communications Physics* thanks the anonymous reviewers for their contribution to the peer review of this work. A peer review file is available.

Reprints and permission information is available at <http://www.nature.com/reprints>

Publisher's note Springer Nature remains neutral with regard to jurisdictional claims in published maps and institutional affiliations.



Open Access This article is licensed under a Creative Commons Attribution 4.0 International License, which permits use, sharing, adaptation, distribution and reproduction in any medium or format, as long as you give appropriate credit to the original author(s) and the source, provide a link to the Creative Commons license, and indicate if changes were made. The images or other third party material in this article are included in the article's Creative Commons license, unless indicated otherwise in a credit line to the material. If material is not included in the article's Creative Commons license and your intended use is not permitted by statutory regulation or exceeds the permitted use, you will need to obtain permission directly from the copyright holder. To view a copy of this license, visit <http://creativecommons.org/licenses/by/4.0/>.

© The Author(s) 2023